# Self-excited oscillations in a collapsible channel, with applications to retinal venous pulsation

Peter S. Stewart*, Alexander J. E. Foss†

July 5, 2019

**Abstract**

We consider a theoretical model for the flow of Newtonian fluid through a long flexible-walled channel which is formed from four compliant and rigid compartments arranged alternately in series. We drive the flow using a fixed upstream flux and derive a spatially one-dimensional model using a flow profile assumption. The compliant compartments of the channel are assumed subject to a large external pressure, so the system admits a highly collapsed steady state. Using both a global (linear) stability eigensolver and fully nonlinear simulations we show that these highly collapsed steady states admit a primary global oscillatory instability similar to observations in a single channel. We also show that in some regions of the parameter space the system admits a secondary mode of instability which can interact with the primary mode and lead to significant changes in the structure of the neutral stability curves. Finally we apply the predictions of this model to the flow of blood through the central retinal vein and examine the conditions required for the onset of self-excited oscillation. We show that the neutral stability curve of the primary mode of instability discussed above agrees well with canine experimental measurements of the onset of retinal venous pulsation, although there is a large discrepancy in the oscillation frequency.

## 1 Introduction

Retinal venous pulsation (RVp) was first described by Coccius [9] and takes the form of a vigorous oscillation in the central retinal vein as it crosses the optic disc. Interestingly, this pulsation is much stronger than the corresponding pulsation in the central retinal artery. Despite years of effort, this surprising observation is still incompletely understood (see [32] for a recent review of the clinical literature). Under healthy conditions the pulsation is present or, if not, can be easily triggered by a mild increase in intraocular pressure (the pressure in the vitreous in the eye, denoted IOP). However, it has long been established that the RVp disappears for a sufficiently large intracranial pressure (the pressure in the brain, denoted ICP) [24, 44] indicating a strong coupling between the pressure environments in the eye and the brain. In addition, spontaneous RVp is also less common in patients with glaucoma [22, 31].

*School of Mathematics and Statistics, The Mathematics and Statistics Building, University Place, University of Glasgow, Glasgow, UK. G12 8SQ

†Department of Ophthalmology, Queens Medical Centre, Nottingham, UK. NG7 2UH

To better quantify these clinical indicators, the onset of RVp has been measured as a function of ICP in animal models by Morgan *et al.* [33]. Their measurements indicate that the onset curve is formed by two branches: for low ICP the critical IOP required for the onset of pulsation is independent of ICP (approx 14.9mmHg in canines [33]) while for larger ICP the critical IOP for pulsation scales linearly with ICP. If such an onset curve could be well validated in humans, it would provide foundation for a novel new non-invasive method to measure ICP since IOP can be adjusted and measured relatively easily. Given a measurement of a patient's IOP at RVp onset, the predicted onset curve could then be used to either verify that the corresponding ICP is in the normal range (if the IOP lies in the flat region of the onset curve) or provide a non-invasive estimate of the ICP (if the IOP lies in the linear region of the onset curve). Several steps in this direction have already been taken (eg. [11, 12, 15]), but theoretical understanding of the coupling between the pressures in the eye and the brain needs to be improved before the method can be used reliably.

The geometry of the central retinal artery and vein as they pass through the optic nerve and into the eye has been well described in a series of classical papers by Hayreh in the 1960s [16,37,38]. The geometry is sketched in Fig. 1(a), showing the course of the vein as it leaves the eye, passes along the optic nerve before exiting into the orbit and then connecting to the ophthalmic vein. As it exits the nerve the vein must cross the optic nerve sheath, which is comprised of meningeal tissue including the optic nerve subarachnoid space (which is filled with CSF at the ICP) confined by the dura mater.

In our previous theoretical work to quantify the onset of RVp we modelled the flow along the retinal vein using a Starling resistor. In particular, we extended the model of Levine [25] to represent the vein as a long flexible-walled channel which is externally surrounded by the IOP and the ICP at different points along its length (see Fig. 1 below). The vein is assumed to be formed of four compartments in series: from the upstream end, the first compartment represents the portion of the vein in the eye (the portion that can be observed through an ophthalmoscope); the second represents the portion of the vein that passes through the lamina cribrosa and along the centre of the optic nerve; the third represents the portion of the vein which crosses the optic nerve sheath and the fourth represents the portion of the vein outside the nerve, connecting downstream to the ophthalmic vein. These sections are labelled in Fig. 1 below. Compartments 1 and 3 are assumed to have flexible walls, with compartment 1 externally surrounded by vitreous at the IOP and compartment 3 externally surrounded by cerebrospinal fluid (CSF) at the ICP. Compartment 2 was assumed to be tightly confined by the nerve fibres and so can be effectively considered to be rigid, while compartment 4 was also modelled as rigid for simplicity. The flow of blood was modelled using the incompressible Navier–Stokes equations while the elastic portions of the channel wall were modelled as a tensioned membrane with an elastic pre-stress. Similar to many previous studies of flow in collapsible vessels (eg. [40, 49]) the flow was simplified using a long-wavelength approximation with a flow profile assumption. The ICP and IOP were chosen to be prescribed functions of time with simple oscillatory profiles. The model parameters could all be reliably estimated from the literature with the exception of the vein wall tension (membrane pre-stress), which was chosen to exhibit transition to oscillatory instability (which we attributed to RVp) at a physiologically realistic value of the IOP. We showed that for physiologically realistic parameter choices the system exhibits a transition to fully nonlinear instability along an onset curve which shows excellent agreement with the measured onset curve in canine experiments [33].

In this study we revisit the model of [42] to examine its behaviour across the parameter space (not just for parameters relevant to RVp). We ignore the time-dependency of the external

pressures and instead treat a model system of flow in a flexible-walled channel with two compliant compartments. In particular, we look for the onset of self-excited oscillations by recasting the governing equations as a linear stability problem about a non-uniform static state. In a similar manner to [40], we construct a global (linear) stability eigensolver which can be solved to isolate the critical conditions for instability with much reduced computational cost compared to full nonlinear simulations of the same system. Such an approach provides explicit access to the corresponding oscillation frequency at neutral stability and elucidates all the normal modes of the system.

This study follows in the spirit of many previous studies of fluid flow in collapsible vessels and the associated onset of self-exited oscillations, pertinent to physiological phenomena such as Korotkoff noises generated during sphygmomanometry, wheezing in the lungs and phonation in the vocal folds. Theoretical models for the onset of these self-excited oscillations span empirical lumped parameter models (eg. [1, 3]), reduced long-wavelength models (eg. [19, 43, 49, 50]) and full numerical computations in channels and tubes (eg. [17, 26, 27, 41]). Comprehensive literature reviews are available elsewhere [13, 18]. Of most pertinent interest to the present study are long-wavelength models for flow through collapsible channels with prescribed inlet flux, where the wall elasticity takes the form of an axial membrane tension [40, 49–51]. These models are similar in spirit to our previous model for the onset of RVp [42], albeit with only one compliant compartment rather than two. For a constant external pressure on the collapsible segment, we previously showed that this collapsible channel system with one flexible compartment admits two distinct families of self-excited oscillation [40]: for low tensions the system admits a family of low-frequency oscillatory modes where the flexible portion of the channel is highly inflated along most of its length, and for large tensions the system admits a family of high-frequency oscillatory modes where the channel is highly collapsed. We now revisit these predictions in a model with two compliant compartments rather than one.

Flow through channels composed of multiple compliant compartments (or over multiple compliant plates) also has potential application in turbulent-drag reduction, where it has been hypothesised that arranging several compliant panels in series could be used as part of a device to delay the onset of laminar-turbulent transition [7, 8, 36], based on initial experiments conducted by Kramer in the 1960s [23].

This paper is arranged as follows. In Sec. 2 we formulate the governing equations and describe the formulation of the global (linear) stability eigensolver. In Sec. 3 we consider the dimensionless model and examine its behaviour across a wide range of the parameter space, using a combination of the linear eigensolver and fully nonlinear simulations. In particular, we find that the system exhibits multiple families of self-excited oscillations, some of which involve strong coupling between the compliant compartments and others which are almost decoupled. In Sec. 4 we use this eigensolver approach to revisit our previous predictions from [42] and examine the consequences of these extra modes of oscillation for the our predictions of RVp onset.

# 2 The model

The model setup considered herein is motivated by blood flow the central retinal vein, similar to that proposed by [42]. However, in this study the external pressures are regarded as both spatially and temporally uniform (rather than oscillatory functions of time driven by fluctuations in arterial pressure) so the system admits a non-uniform static wall configuration. We test the stability of this static state using a global (linear) eigensolver and can thus make progress in systematically

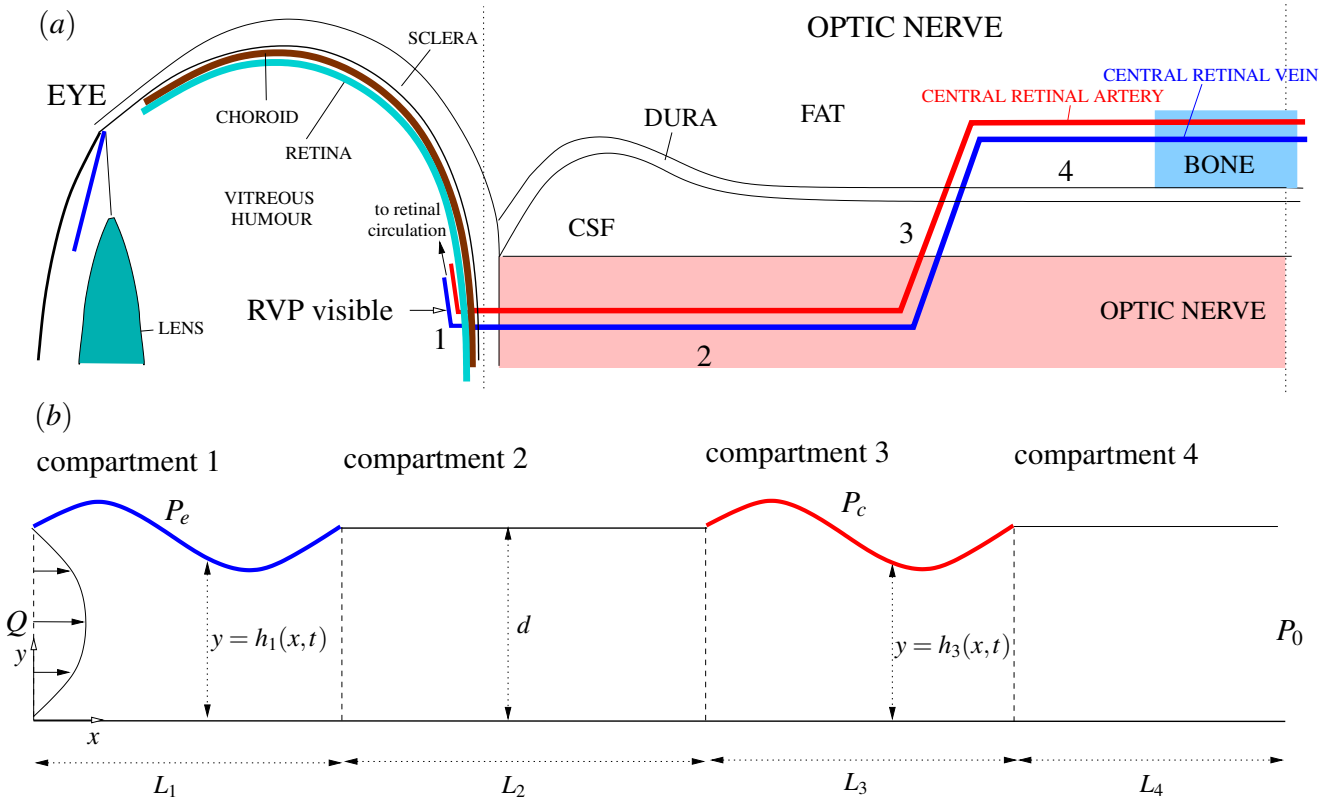


Figure 1: (a) Sketch of the course of the central retinal vein as it exits the eye and passes through the optic nerve highlighting the four compartments of interest labelled 1-4; (b) Setup of the mathematical model in dimensional variables, showing the four compartments of the channel arranged in series.

exploring the parameter space with much reduced computational cost. We then apply this model to the particular setup in the central retinal vein to examine the onset of oscillations in this geometry, which explains some of the clinically observed features of RVp.

We consider a geometry inspired by the central retinal vein composed of four compartments in series (labelled on Fig. 1a), arranged in an identical manner to [42], as shown in Fig. 1(b). In particular we consider flow in a rigid walled-channel of constant width $d$ where two distinct portions of the upper wall (of lengths $L_1$ and $L_3$) have been replaced by a flexible membrane. A rigid segment (of length $L_2$) spans between the two compliant segments, and there is a further rigid segment (of length $L_4$) downstream. The channel geometry is described using Cartesian coordinates $(x, y)$, where $x$ is the distance measured along the channel axis from the upstream inlet and $y$ is the perpendicular distance from the lower wall of the channel. We consider corresponding unit vectors $\mathbf{e}_x$ and $\mathbf{e}_y$. Time is denoted $t$. The inlet to the upstream compliant compament is denoted $x = 0$, where we prescribe boundary conditions on the flow.

The flow is assumed to be homogeneous and Newtonian of (constant) viscosity and density denoted $\mu$ and $\rho$, respectively.

Similar to some Starling Resistor experiments (eg [4, 5]), we prescribe the fluid flux $Q$ at the channel inlet ($x = 0$) and the pressure at the channel outlet $P_0$ ($x = L_1 + L_2 + L_3 + L_4$). This

work builds on several previous theoretical studies of flow-driven oscillations through a channel with a single flexible compartment along its length (eg. [40, 49, 50]).

The elastic portions of the wall are assumed to exhibit a tensile pre-stress $T$ (or membrane tension) acting axially along the channel (see discussion in [6]) similar to many previous studies of collapsible channel flow (eg. [20, 26, 27, 40, 43]). The influence of other elastic restoring forces, such as bending stiffness, wall inertia and damping have been ignored for simplicity. In general, the channel wall is assumed to be located at position $y = h(x, t)$ while in the rigid segments we have $y = d$ uniformly.

The flexible compartments (denoted 1 and 3) are externally surrounded by another fluid, which is assumed to have uniform pressure: the pressure external to compartment 1 is denoted $P_e$, while the pressure external to compartment 3 is denoted $P_c$.

## 2.1 Non-dimensional variables

To reduce the number of model parameters we non-dimensionalise all lengths on the channel width $d$, velocities on the baseline flow velocity $U_0 = Q/d$ (based on the inlet flux), time on $d/U_0$ and pressures according to the inertial pressure scale

$$p = \rho U_0^2 \tilde{p} + P_0, \tag{1}$$

where $p$ is the dimensional pressure. All dimensionless variables take the same symbol as the dimensional equivalent but denoted with a tilde. This choice of non-dimensionalisation results in the following dimensionless groups

$$\tilde{\mathcal{L}}_1 = \frac{L_1}{d}, \qquad \tilde{\mathcal{L}}_2 = \frac{L_2}{d}, \qquad \tilde{\mathcal{L}}_3 = \frac{L_3}{d}, \qquad \tilde{\mathcal{L}}_4 = \frac{L_4}{d}, \qquad \tilde{\mathcal{R}} = \frac{\rho U_0 d}{\mu}, \tag{2}$$

representing the four dimensionless lengths of the compartments and the Reynolds number $\tilde{\mathcal{R}}$ measuring the relative importance of inertial effects to viscous effects in the flow. Furthermore, we have the non-dimensional external pressures (both assumed spatially and temporally uniform), written as

$$p_e = \frac{P_e - P_0}{\rho U_0^2}, \qquad p_c = \frac{P_c - P_0}{\rho U_0^2}, \tag{3}$$

respectively.

Hence, in dimensionless variables the channel wall is located at $\tilde{y} = \tilde{h}(\tilde{x}, \tilde{t})$, while the dimensionless flow velocity $\tilde{\mathbf{u}} = \tilde{u}(\tilde{x}, \tilde{y}, \tilde{t})\mathbf{e}_x + \tilde{v}(\tilde{x}, \tilde{y}, \tilde{t})\mathbf{e}_y$ and the dimensionless pressure $\tilde{p}(\tilde{x}, \tilde{y}, \tilde{t})$ follow the non-dimensional Navier–Stokes equations

$$\tilde{\nabla} \cdot \tilde{\mathbf{u}} = 0, \qquad \frac{\partial \tilde{\mathbf{u}}}{\partial \tilde{t}} + \tilde{\mathbf{u}} \cdot \tilde{\nabla} \tilde{\mathbf{u}} = -\tilde{\nabla} \tilde{p} + \tilde{\mathcal{R}}^{-1} \tilde{\nabla}^2 \tilde{\mathbf{u}}, \qquad (0 \le \tilde{x} \le \tilde{\mathcal{L}}_1 + \tilde{\mathcal{L}}_2 + \tilde{\mathcal{L}}_3 + \tilde{\mathcal{L}}_4,\ 0 \le \tilde{y} \le \tilde{h}), \tag{4}$$

where the tilded gradient operator $\tilde{\nabla}$ is defined in (dimensionless) Cartesian coordinates. We henceforth drop tildes for notational convenience.

## 2.2 Long-wavelength approximation

Since all four compartments of the vein are typically long compared to the channel width, we reduce the complexity of the system using a long-wavelength approximation (similar to previous

one-dimensional models such as [40, 43]). We construct a small parameter $\epsilon = 1/\mathcal{L}_1 \ll 1$ and rescale the variables according to

$$x = \epsilon^{-1}\breve{x}, \qquad t = \epsilon^{-1}\breve{t}, \qquad v = \epsilon\breve{v}, \tag{5}$$

and the model parameters according to

$$\breve{\mathcal{R}} = \epsilon\mathcal{R}, \qquad \breve{\mathcal{L}}_2 = \epsilon\mathcal{L}_2, \qquad \breve{\mathcal{L}}_3 = \epsilon\mathcal{L}_3, \qquad \breve{\mathcal{L}}_4 = \epsilon\mathcal{L}_4. \tag{6}$$

Dropping breves and neglecting terms of $O(\epsilon^2)$, the final system of equations can be written as ($j = 1, \cdots, 4$).

$$\frac{\partial u_j}{\partial x} + \frac{\partial v_j}{\partial y} = 0, \tag{7a}$$

$$\frac{\partial u_j}{\partial t} + u_j\frac{\partial u_j}{\partial x} + v_j\frac{\partial u_j}{\partial y} = -\frac{\partial p_j}{\partial x} + \frac{1}{\mathcal{R}}\frac{\partial^2 u_j}{\partial y^2}, \tag{7b}$$

$$\frac{\partial p_j}{\partial y} = 0. \tag{7c}$$

These equations are subject to kinematic and no-slip boundary conditions on the elastic sections of the wall in the form,

$$v_j = \frac{\partial h_j}{\partial t}, \qquad u_j = 0, \qquad (y = h_j), \qquad (j = 1, 3), \tag{7d}$$

as well as a balance of normal stress to determine the position of the flexible wall, considered in Sec. 2.4 below. We also impose no-slip boundary conditions on the rigid sections of the wall in the form,

$$u_j = v_j = 0, \qquad (j = 2, 4). \tag{7e}$$

These equations are further coupled to boundary conditions of prescribed inlet flux and zero outlet pressure, in the form

$$\int_0^{h_1(0,t)} u_1(0,t)\,\mathrm{d}y = 1, \qquad p_4(1 + \mathcal{L}_2 + \mathcal{L}_3 + \mathcal{L}_4, t) = 0, \tag{7f}$$

as well as conditions matching the flux and pressure between each compartment.

## 2.3 Integral approximation

Integrating the axial momentum equation (7b) across the cross-section of the channel and applying the boundary conditions (7d,7e), we express the long-wavelength governing equations (7) as a coupled system in terms of three dependent variables in each compartment $u_j$, $h_j$ and $p_j$ ($j = 1, \cdots, 4$), in the form

$$\frac{\partial h_j}{\partial t} + \frac{\partial}{\partial x}\left(\int_0^{h_j} u_j\,\mathrm{d}y\right) = 0, \tag{8a}$$

$$\frac{\partial}{\partial t}\left(\int_0^{h_j} u_j\,\mathrm{d}y\right) + \frac{\partial}{\partial x}\left(\int_0^{h_j} u_j^2\,\mathrm{d}y\right) = -h_j\frac{\partial p_j}{\partial x} + \frac{1}{\mathcal{R}}\left[\frac{\partial u_j}{\partial y}\right]_0^{h_j}. \tag{8b}$$

We denote the flux of blood along the vein through any cross-section of the channel orthogonal to $\mathbf{e}_x$ as

$$q_j(x,t) = \int_0^{h_j} u_j\,\mathrm{d}y, \qquad (j = 1, \cdots, 4). \tag{9}$$

## 2.4 Wall elasticity

We consider the elastic response to wall displacement from the uniform state ($y = d$), where a (long-wavelength) balance of normal stress on the flexible wall gives

$$p_j = \overline{p}_j - \mathcal{T}\frac{\partial^2 h_j}{\partial x^2}, \qquad (j = 1, 3), \tag{10a}$$

where $\overline{p}_j$ is the dimensionless external pressure on compartment $j$ (so $\overline{p}_1 = p_e$ and $\overline{p}_3 = p_c$) where $\mathcal{T}$ is the dimensionless wall tension parameter, defined as

$$\mathcal{T} = \frac{\epsilon^2 T}{\rho U_0^2 d}. \tag{10b}$$

This model (10a) assumes dominance of the longitudinal pre-stress tension and neglects other features such as bending stiffness, wall dissipation and the influence of normal viscous stresses. Furthermore, if an identical approach were applied to a flexible tube this would neglect tensile forces arising from radial and azimuthal deformations of the wall. However, such an assumption is consistent with earlier studies of flow in collapsible tubes which argued that regions of the tube cross-section in which longitudinal tension will have most effect are approximately parallel-sided [6, 29]. This approximation is also consistent with the reduced wall model derived from shell theory in a series of papers by Whittaker and coworkers (eg [45]).

## 2.5 Closure condition

However, this long-wavelength system of equations (7,10a) is not closed. In the literature on collapsible tubes a number of approaches are used to close the system based on specific assumptions or empirical measurements (see extended discussion in [6]). Similar to many previous studies of flow in collapsible channels (*eg.* [40, 43, 49–51]) we close the system of governing equations by assuming the flow profile to be everywhere parabolic (a von Karman–Pohlhausen approximation), in the form

$$u_j(x, y, t) = \frac{6 q_j y(h_j - y)}{h_j^3}, \qquad (j = 1, \cdots, 4), \tag{11}$$

where the system of governing equations (8) in each region becomes

$$\frac{\partial h_j}{\partial t} + \frac{\partial q_j}{\partial x} = 0, \qquad \frac{\partial q_j}{\partial t} + \frac{6}{5}\frac{\partial}{\partial x}\left(\frac{q_j^2}{h_j}\right) = -h_j\frac{\partial p_j}{\partial x} - \frac{12}{\mathcal{R}}\frac{q_j}{h_j^2}, \qquad (j = 1, \cdots, 4). \tag{12a}$$

The fluid pressure in the compliant regions (compartments 1, 3) of the channel follows directly from the normal stress balance (10a). Conversely, in the rigid segments (compartments 2,4) we assume the channel width is equal to the baseline width and set $h_j = 1$ ($j = 2, 4$), so that the flux follows as ($j = 2, 4$)

$$\frac{\partial q_j}{\partial x} = 0, \qquad \frac{\partial q_j}{\partial t} = -\frac{\partial p_j}{\partial x} - \frac{12}{\mathcal{R}} q_j. \tag{13}$$

Hence, the fluid flux through the rigid segments is independent of $x$ and we can integrate the momentum equation along the rigid sections to obtain an expression for the pressure along the

compartment, from which we can deduce boundary conditions for the flow in the compliant segments.

In summary, the governing equations in the compliant segments of the channel can be written in the closed form ($j = 1, 3$)

$$\frac{\partial h_j}{\partial t} + \frac{\partial q_j}{\partial x} = 0, \tag{14a}$$

$$\frac{\partial q_j}{\partial t} + \frac{6}{5}\frac{\partial}{\partial x}\left(\frac{q_j^2}{h_j}\right) = \mathcal{T} h_j \frac{\partial^3 h_j}{\partial x^3} - \frac{12}{\mathcal{R}}\frac{q_j}{h_j^2}. \tag{14b}$$

Matching the fluid flux and pressure at the junctions between each segment of the channel, and applying the downstream pressure boundary condition (7f), we obtain eight boundary conditions on the compliant compartments in the form

$$q_1(0,t) = 1, \qquad q_1(1,t) = q_3(1+\mathcal{L}_2, t), \tag{14c}$$

$$h_1(0,t) = h_1(1,t) = h_3(1+\mathcal{L}_2,t) = h_3(1+\mathcal{L}_2+\mathcal{L}_3,t) = 1, \tag{14d}$$

$$\mathcal{T}\frac{\partial^2 h_1}{\partial x^2}(1,t) - \mathcal{T}\frac{\partial^2 h_3}{\partial x^2}(1+\mathcal{L}_2,t) = p_e - p_c - \mathcal{L}_2\left(\frac{\partial q_1}{\partial t}(1,t) + \frac{12}{\mathcal{R}}q_1(1,t)\right), \tag{14e}$$

$$\mathcal{T}\frac{\partial^2 h_3}{\partial x^2}(1+\mathcal{L}_2+\mathcal{L}_3,t) = p_c - \mathcal{L}_4\left(\frac{\partial q_3}{\partial t}(1,t) + \frac{12}{\mathcal{R}}q_3(1,t)\right). \tag{14f}$$

The system (14) is closed, and is almost identical to the system derived by [42].

## 2.6 Static configuration

Following previous studies of collapsible channel flow (eg [40, 43]) we compute the corresponding static configuration of the system by solving the time-independent version of (14), denoting this solution with the superscript $(s)$. We note that the static system must have unit flux everywhere along the channel for this choice of upstream boundary conditions. Nonlinear solutions of the resulting seventh-order system of one-dimensional ODEs are computed using Newton's method. In the results below we summarise simulations by the minimal and maximal constriction of the static wall in each compliant compartment.

## 2.7 Global linear stability eigensolver

A global linear stability eigensolver for collapsible channel flow subject to a large external pressure was recently presented by [40]. We follow a similar approach here, considering the time-dependent behaviour of a small perturbation from the static configuration identified in Sec. 2.6. We linearise the system of equations around this static state and look for exponentially growing solutions in time. For the collapsible channel model (14) we expand the dependent variables according to

$$(h_1(x,t), h_2(x,t), q_1(x,t), q_2(x,t)) = (h_1^{(s)}, h_2^{(s)}, 1, 1) + \delta(\hat{h}_1(x), \hat{h}_2(x), \hat{q}_1(x), \hat{q}_2(x))\mathrm{e}^{\sigma t} + O(\delta^2), \tag{15}$$

where $\delta \ll 1$, $\sigma \in \mathbb{C}$ is the complex growth rate of the system and hatted variables are the complex eigenfunctions. Neglecting terms of $O(\delta^2)$, the linearised system becomes ($j = 1, 3$),

$$\sigma \hat{h}_j + \frac{\partial \hat{q}_j}{\partial x} = 0, \tag{16a}$$

$$\sigma \hat{q}_j + \frac{6}{5}\frac{\partial}{\partial x}\left(\frac{2\hat{q}_j}{h_j^{(s)}} - \frac{1}{(h_j^{(s)})^2}\frac{\partial \hat{h}_j}{\partial x}\right) = \mathcal{T} h_j^{(s)} \frac{\partial^3 \hat{h}_j}{\partial x^3} + \mathcal{T}\hat{h}_j \frac{\partial^3 h_j^{(s)}}{\partial x^3} - \frac{12}{\mathcal{R}}\left(\frac{\hat{q}_j}{(h_j^{(s)})^2} - \frac{2\hat{h}_j}{(h_j^{(s)})^3}\right), \tag{16b}$$

where we have used (16a) in (16b) to reduce to a system linear in $\sigma$. These equations are subject to the linearised boundary conditions in the form,

$$\hat{q}_1(0) = 0, \qquad \hat{q}_1(1) = \hat{q}_3(1 + \mathcal{L}_2), \tag{16c}$$

$$\hat{h}_1(0) = \hat{h}_1(1) = \hat{h}_3(1 + \mathcal{L}_2) = \hat{h}_3(1 + \mathcal{L}_2 + \mathcal{L}_3) = 0, \tag{16d}$$

$$\mathcal{T}\frac{\partial^2 \hat{h}_1}{\partial x^2}(1) - \mathcal{T}\frac{\partial^2 \hat{h}_3}{\partial x^2}(1 + \mathcal{L}_2) = -\mathcal{L}_2\left(\sigma \hat{q}_1(1) + \frac{12}{\mathcal{R}}\hat{q}_1(1)\right), \tag{16e}$$

$$\mathcal{T}\frac{\partial^2 \hat{h}_3}{\partial x^2}(1 + \mathcal{L}_2 + \mathcal{L}_3) = -\mathcal{L}_4\left(\sigma \hat{q}_3(1 + \mathcal{L}_2 + \mathcal{L}_3) + \frac{12}{\mathcal{R}}\hat{q}_3(1 + \mathcal{L}_2 + \mathcal{L}_3)\right). \tag{16f}$$

We solve the linear system (16) numerically using an approach identical to [40]. As a brief summary, the two spatial domains ($0 \leq x \leq 1$ and $1 + \mathcal{L}_2 \leq x \leq 1 + \mathcal{L}_2 + \mathcal{L}_3$) are each discretised onto a uniformly-spaced grid. The governing equations and boundary conditions (16) are mapped onto these grids by approximating spatial derivatives using second-order finite differences. What follows is a matrix eigenvalue problem for the complex growth rate $\sigma$ with the associated (discretised) eigenfunctions $\tilde{h}_1(x;\sigma)$, $\tilde{h}_3(x;\sigma)$, $\tilde{q}_1(x;\sigma)$ and $\tilde{q}_3(x;\sigma)$. Interested readers are referred to [40] for more details on the construction of the eigensolver.

In particular we isolate neutral stability curves of the system (where $\mathrm{Re}(\sigma) = 0$) using a bisection method. At neutral stability we denote $\sigma = \pm i\omega$, where $\omega$ is the dimensionless oscillation frequency. In Sec. 4 the corresponding dimensional oscillation frequency is denoted as $\Omega = \omega U_0/L_1$, measured in Hz.

## 2.8 Fully nonlinear simulations

Fully nonlinear simulations of the governing equations (14) are constructed using the numerical scheme described and used previously by [42], based on a semi-implicit finite difference method which is first order in time and fourth-order in space.

In fully nonlinear simulations we quantify the solution in terms of the timetraces of either of the midpoint of the spatial profile, denoted $\mathrm{mid}(\,\cdot\,)$ or by the maximal constriction of the flexible wall across the compartments denoted $h_{mj} = \min_x(h_j)$ for $j = 1, 3$. Alternatively, in constructing bifurfaction diagrams we use the oscillation amplitude of the compartment midpoint which we calculate as

$$A_j = \max_t\left(\mathrm{mid}(h_j - h_j^{(s)})\right) - \min_t\left(\mathrm{mid}(h_j - h_j^{(s)})\right), \qquad (j = 1, 3), \tag{17}$$

where the subscript $t$ represents taking the maximum or minimum over a period of fully saturated oscillation.

### 2.9 Baseline parameters for the onset of retinal pulsation

In Sec. 4 below we apply the model to the particular geometry of the central retinal vein in an attempt to explain the onset of the retinal venous pulse. The dimensional parameters for the model are listed in Table 1.

Most of the model parameters can be estimated reliably from the literature. In particular, the geometry of the vein has been well characterised [16, 37, 38, 48] and the baseline diameter and lengths of the compartments are listed in Table 1, which translates into dimensionless segment lengths $\mathcal{L}_2 = 10$, $\mathcal{L}_3 = 1$ and $\mathcal{L}_4 = 10$.

The inlet flux of blood entering the vein is the retinal blood flow which has been measured in experiments (eg [10]). Herein we adopt a baseline value of 44 $\mu$ l min$^{-1}$ [10]. The corresponding mean velocity of blood along the vein has been measured in the range 2-6 cm s$^{-1}$ from which we estimate a baseline value of $U_0$=4 cm s$^{-1}$ [46]. This translates into a baseline vein diameter (and hence channel width) of $d \approx 152.8\mu m$ [42].

In addition, the density and viscosity of blood are well-known [34]. For the baseline parameter values this translates into a reduced Reynolds number of $\mathcal{R} = 0.245$.

In particular, compartment 1 is externally surrounded by vitreous at the IOP, denoted by $P_e$ in the model. Also, compartment 3 is externally surrounded by CSF at the ICP, denoted $P_c$ in the model. The remaining two compartments are assumed to be rigid. In compartment 2, this is appropriate because the blood vessels are tightly surrounded by axonal nerve fibres (which in themselves can be assumed rigid [2]), severely limiting deformation. In compartment 4 this assumption is made for simplicity, but since the tissue pressure in the fat external to the vessel is significantly less than the IOP ($\lesssim$ 3mmHg), assuming this region was compliant would not contribute to the oscillatory behaviour significantly. In normal adults the IOP is measured in the range 10-35mmHg while the ICP is measured in the range 0-20mmHg, depending on position.

We approximate the vein outlet pressure $P_0$ as the orbital venous pressure (OVP): this pressure is extremely difficult to measure in humans, but we expect it to be close to the orbital tissue pressure which is measured in humans in the range $\lesssim$ 2.6mmHg [33]. In our results in Sec. 4 below we simply report all pressures as a difference to the OVP.

The elastic pre-stress (tension) in the vein wall can only be obtained *in vivo* and has not been reliably measured to the best of our knowledge. In our previous study we used a baseline of $T = 0.110$ N m$^{-1}$, which corresponds to a dimensionless value of $\mathcal{T} = 10$ in conjunction with the other baseline parameter values listed in Table 1. We explore the behaviour across a range of dimensionless tensions in Fig. 8 below.

Results pertinent to these parameter values (Sec. 4) are reported in terms of dimensional variables for ease of physiological interpretation.

## 3 Results

In this section we explore the general properties of the dimensionless model outlined in Sec. 2. In particular, we outline the structure of the static solutions (Sec. 3.1) and then explore the onset of self-excited oscillations from this static state using both the global linear stability eigensolver and also fully nonlinear simulations (Sec. 3.2).

For breveity, in all cases we consider the lengths of the compartments set at $\mathcal{L}_2 = \mathcal{L}_4 = 10$ and $\mathcal{L}_3 = 1$. We hence only vary the (dimensionless) membrane tension $\mathcal{T}$, the Reynolds number $\mathcal{R}$ and the dimensionless external pressures $p_e$ and $p_c$.

| Parameter | Symbol | Value | Unit | Source |
|---|---|---|---|---|
| Blood viscosity | $\mu$ | 0.004 | Pa·s | [34] |
| Blood density | $\rho$ | 1000 | kg m$^{-3}$ | [34] |
| Length of compartment 1 | $L_1$ | $10^{-3}$ | m | [30] |
| Length of compartment 2 | $L_2$ | $10^{-2}$ | m | [37] |
| Length of compartment 3 | $L_3$ | $10^{-3}$ | m | [48] |
| Length of compartment 4 | $L_4$ | $10^{-2}$ | m | estimated |
| Retinal blood flow | $Q$ | 44 | $\mu$ l min$^{-1}$ | [10] |
| Baseline blood velocity | $U_0$ | 4 | cm s$^{-1}$ | [46] |
| Vein diameter | $d$ | $152 \times 10^{-6}$ | m | estimated |
| ICP | $P_e$ | 10-35 | mmHg | |
| IOP | $P_c$ | 0-20 | mmHg | |
| OVP | $P_0$ | $\lesssim$2.6 | mmHg | [33] |
| Vein wall tension | $T$ | 0.110 | N m$^{-1}$ | [42] |

Table 1: Typical dimensional parameter values for the model.

## 3.1 Static wall profiles

Since the flux must be constant along the entire channel length for a time-independent solution ($q = 1$), for $p_c$ fixed the static solution in compartment 3 satisfies the reduced model

$$\frac{6}{5}\frac{\partial}{\partial x}\left(\frac{1}{h_3^{(s)}}\right) = \mathcal{T} h_3^{(s)} \frac{\partial^3 h_3^{(s)}}{\partial x^3} - \frac{12}{\mathcal{R}} \frac{1}{(h_3^{(s)})^2}, \tag{18a}$$

$$h_3^{(s)}(1+\mathcal{L}_2, t) = h_3^{(s)}(1+\mathcal{L}_2+\mathcal{L}_3, t) = 1, \qquad \mathcal{T}\frac{\partial^2 h_3^{(s)}}{\partial x^2}(1+\mathcal{L}_2+\mathcal{L}_3, t) = p_c - \mathcal{L}_4 \frac{12}{\mathcal{R}}. \tag{18b}$$

which is closed and independent of $p_e$ and the profile in compartment 1; this model is identical to the static model of a single compartment collapsible channel considered by [40]. For this choice of global boundary conditions (prescribed flux at the inlet, prescribed pressure at the outlet) in the static version of the problem the downstream rigid compartment is completely decoupled. Conversely, the static solution in compartment 1 satisfies the reduced model

$$\frac{6}{5}\frac{\partial}{\partial x}\left(\frac{1}{h_1^{(s)}}\right) = \mathcal{T} h_1^{(s)} \frac{\partial^3 h_1^{(s)}}{\partial x^3} - \frac{12}{\mathcal{R}} \frac{1}{(h_1^{(s)})^2}, \tag{18c}$$

$$h_1^{(s)}(0, t) = h_1^{(s)}(1, t) = 1, \qquad \mathcal{T}\frac{\partial^2 h_1^{(s)}}{\partial x^2}(1, t) - \mathcal{T}\frac{\partial^2 h_3^{(s)}}{\partial x^2}(1+\mathcal{L}_2, t) = p_e - p_c - \mathcal{L}_2 \frac{12}{\mathcal{R}}. \tag{18d}$$

which couples to $p_e - p_c$ and also to the (linearised) membrane curvature compartment 3. Hence, the behaviour in the upstream compliant compartment will be coupled to the behaviour in compartment 3.

To further explore the coupling between the static wall profiles, in Fig. 2 we plot the maximal and minimal channel widths in each compartment as a function of $\mathcal{T}$ holding $p_e = 275$ and $p_c = 100$ for a variety of Reynolds numbers. Similar to [40], for sufficiently low $\mathcal{R}$ the static profile in each compartment is unique for each $\mathcal{T}$, with the channel approximately uniform for large $\mathcal{T}$ and becoming more collapsed as $\mathcal{T}$ decreases due to the Bernoulli effect (see profiles for

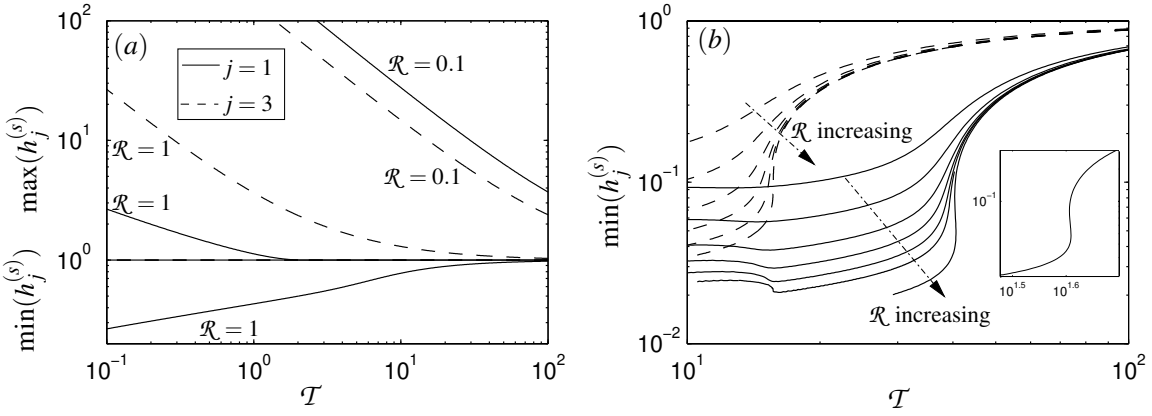


Figure 2: Summary of static wall profiles for $p_c = 100$ and $p_e = 275$ summarising the maximal and minimal channel widths as a function of the wall tension $\mathcal{T}$ for a variety of $\mathcal{R}$, showing compartment 1 (3) as a solid (dashed) line: (a) low Reynolds numbers $\mathcal{R} = 0.1$ and $\mathcal{R} = 1$; (b) larger Reynolds numbers $\mathcal{R} = 10, 25, 50, 75, 100, 125, 200$. The inset in (b) shows a close-up of the curve for $\mathcal{R} = 200$, highlighting the three static states for a range of $\mathcal{T}$. Here $\mathcal{L}_2 = \mathcal{L}_4 = 10$ and $\mathcal{L}_3 = 1$.

$\mathcal{R} = 0.1$ and $\mathcal{R} = 1$ in Fig. 2). For larger $\mathcal{R}$ (see Fig. 2b) the profile in each compartment becomes increasingly collapsed and the system exhibits multiple static states for a range of $\mathcal{T}$ (these ranges are distinct between the two compartments), with each exhibiting two stable solutions with an unstable intermediate state. Self-excited oscillations occur from the most collapsed static branch (similar to [40]).

## 3.2 Onset of self-excited oscillations

For each point in the parameter space static solutions to (14) are isolated numerically and the corresponding global stability problem about this static state (16) is solved as a matrix problem to generate $\sigma \in \mathbb{C}$. We isolate neutrally stable solutions *ie.* parameter combinations where the global growth rate of the system is purely imaginary ($\mathrm{Re}(\sigma) = 0$).

We consider several slices through the parameter space. Firstly, we consider fixed (dimensionless) membrane tension and Reynolds number and consider the onset of instability in the parameter space spanned by the two external pressures (Sec. 3.2.1). Secondly, we consider fixed external pressures and consider the parameter space spanned by membrane tension and Reynolds number (Sec. 3.2.2).

### 3.2.1 Onset of oscillatory instability for fixed tension and Reynolds number

As a baseline case we consider the point in parameter space with $\mathcal{T} = 1$ and $\mathcal{R} = 1$, in Fig. 3(a) we trace the neutral stability curves of the most unstable modes in the space spanned by the two external pressures. The system is stable for low $p_c$ and low $p_e$ as expected. For larger pressures we trace two distinct neutral stability curves which almost intersect at $p_c \approx 150$ and $p_e \approx 300$. Note that the system does not subsequently restabilise across the rightmost curve but the system is simply unstable to two modes of oscillation rather than one.

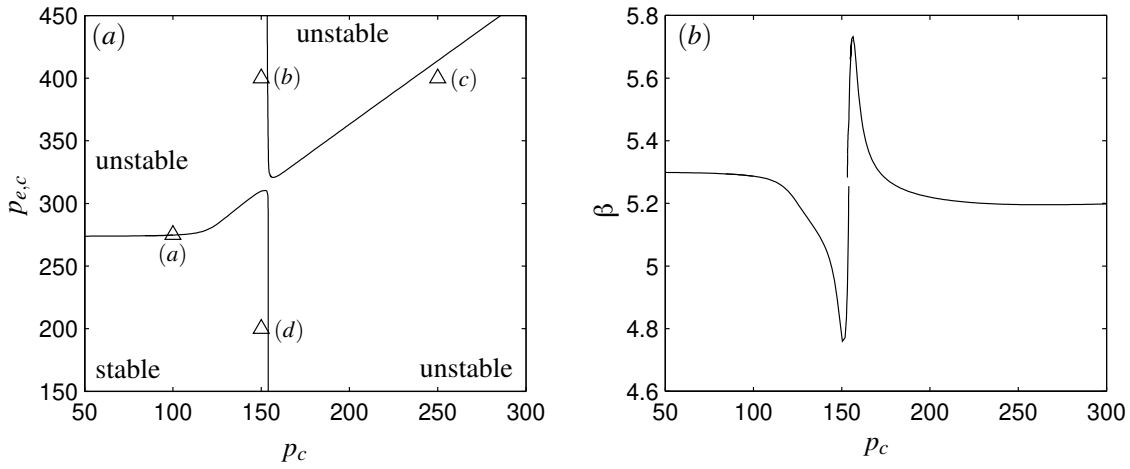


Figure 3: Neutrally stable oscillations of the system for fixed (dimensionless) membrane tension and Reynolds number: (a) neutral stability curves showing the critical value of $p_e$ required for oscillation as a function of $p_c$; (b) associated oscillation frequencies plotted against $p_c$. Here $\mathcal{T} = 1$, $\mathcal{R} = 1$, $\mathcal{L}_2 = \mathcal{L}_4 = 10$ and $\mathcal{L}_3 = 1$.

In the far-field (far from the interaction) two branches of the neutral curves are approximately independent of $p_e$ (close to the points labelled (b) and (d) in Fig. 3a) and depend only on the value of $p_c \approx 150$. In addition, for low $p_c$ there is a branch of oscillations which onset for approximately constant $p_e$ (close to the point labelled (a) in Fig. 3a), and for large $p_c$ there is a branch of oscillations where the critical $p_e$ increases linearly with $p_c$ (close to the point labelled (c) in Fig. 3a). These latter two branches exhibit strong qualitative similarity to the experimental measurements of RVp onset [33], as discussed in Sec. 4. The accompanying frequencies of neutral stability oscillation are shown in Fig. 3(b). Interestingly the two branches exhibit similar frequencies close to their intersection, reminiscent of a modal interaction. Also, as $p_c$ becomes large or small these frequencies asymptote to a constant value.

### 3.2.2 Fully nonlinear oscillations

To assess the fully nonlinear behaviour of the system associated with these neutral curves, in Fig. 4 we consider the growth of instability at two distinct points just inside the unstable regime. In particular we consider two points where the system transitions from globally stable to unstable, close to the points labelled (a) and (d) in Fig. 3.

Firstly, at the point labelled (a) in Fig. 3, just inside the unstable region across the neutral curve with constant critical $p_e$, the fully nonlinear oscillation in the compartment midpoint (Fig. 4a) has comparable amplitude in both compliant segments. This feature is also evident in the bifurcation diagram constructed based on the amplitude of oscillation of the compartment midpoint (Fig. 4b) for a range of $p_c$ beyond the critical value (marked with an $\times$). The onset of instability is clearly supercritical, in line with previous studies of flow-driven oscillations in collapsible channels [40]. We term this mode of instability (i) and note that it involves oscillations of significant amplitude in both compliant compartments.

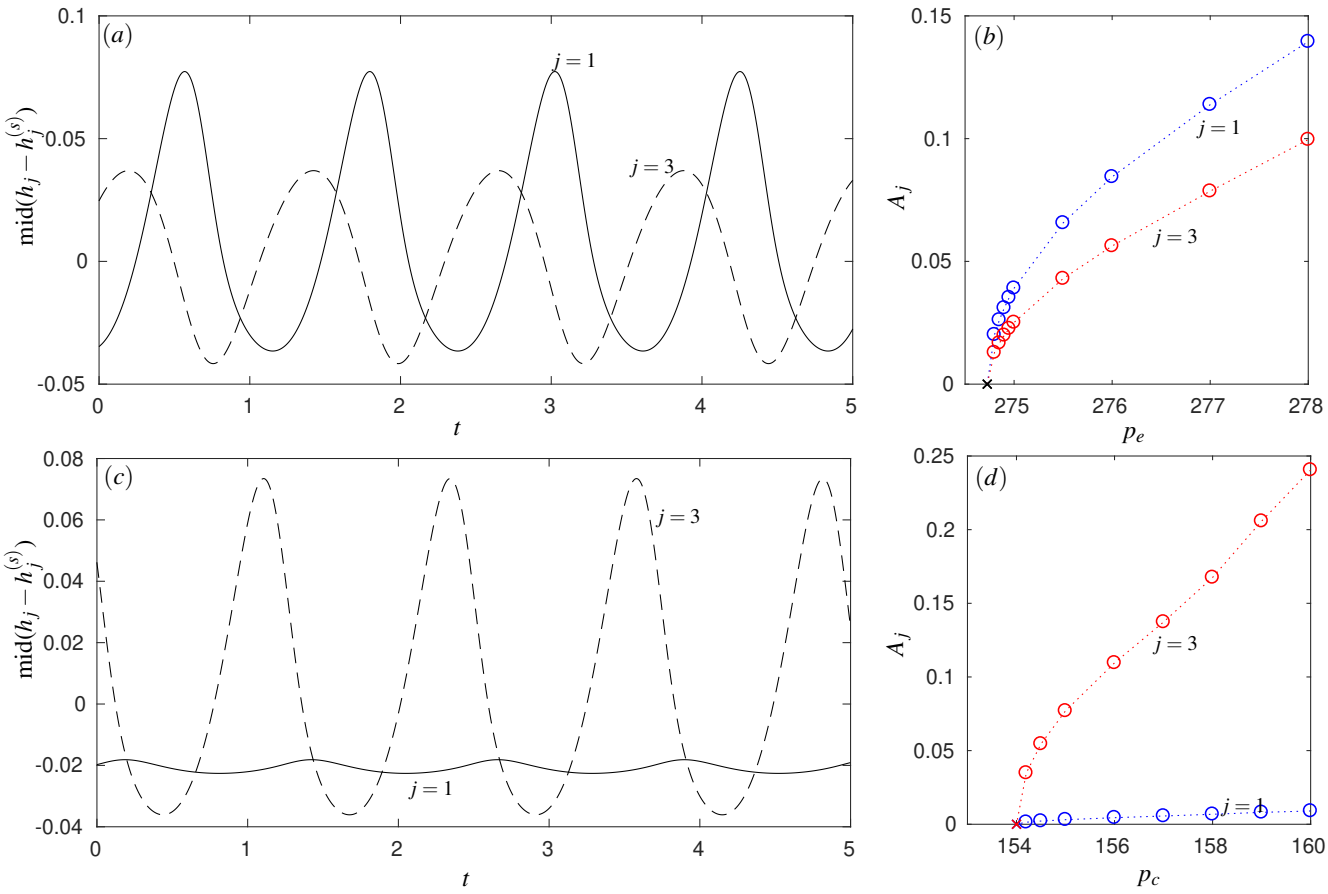


Figure 4: Fully nonlinear oscillations of the system for fixed (dimensionless) membrane tension and Reynolds number: (a) timetrace of the compartment midpoint for $p_e = 277$, $p_c = 100$; (b) bifurcation diagram showing the amplitude of the oscillation of each compartment midpoint as a function of $p_e$ for $p_c = 100$; (c) timetrace of the compartment midpoint for $p_e = 275$, $p_c = 156$; (d) bifurcation diagram showing the amplitude of the oscillation of each compartment midpoint as a function of $p_c$ for $p_e = 275$. Here $\mathcal{T} = 1$, $\mathcal{R} = 1$, $\mathcal{L}_2 = \mathcal{L}_4 = 10$ and $\mathcal{L}_3 = 1$.

Conversely, close to the point labelled (d) in Fig. 3, just inside the unstable region across the neutral curve with constant critical $p_c$, the fully nonlinear oscillation in the compartment midpoint is of significantly larger amplitude in the downstream compliant segment compared to the upstream (Fig. 4c). The feature is also evident in the bifurcation diagram constructed based on the amplitude of oscillation of the compartment midpoints (Fig. 4d) for a range of $p_e$ beyond the critical value (marked with an $\times$). Hence, this branch of oscillations is strongly dominated by the downstream compliant compartment and the upstream compartment is almost perfectly decoupled, which is further enhanced as the length of the intermediate rigid segment ($\mathcal{L}_2$) increases. We term this mode of instability (ii) and note that it (predominantly) involves large amplitude oscillations in compartment 3 only and its onset is (essentially) independent of the value of $p_e$.

It is evident that the saturated oscillations in both cases exhibit a significant modification to the mean position of the membrane midpoint over a period of oscillation (Fig. 4a,c). This change in the mean position of the membrane reflects a net exchange of mass between the compartments. In Fig. 4(a) the nonlinear oscillation drives mass into compartment 1 at the expense of compartment 2 over a period, while in Fig. 4(c) the nonlinear oscillation drives mass into compartment 1 at the expense of compartment 2 over a period.

### 3.2.3 Onset of oscillatory instability for fixed external pressures

To assess the structure of the neutral stability curves in the parameter space spanned by membrane tension and Reynolds number, in Fig. 5 we consider four distinct choices of the external pressures (marked as open triangles in Fig. 3). The corresponding neutral curves all exhibit a similar structure, with two independent branches of oscillation which are labelled (i) and (ii) corresponding to the modes identified above, shown as solid and dashed lines respectively. The most unstable branch varies across the parameter space, with (i) more unstable in Fig. 5(a,b) and (ii) more unstable in Fig. 5(c,d). Each branch of oscillation is similar in structure to the primary branch of instability predicted in flow-driven oscillations through a flexible channel with a single compartment [40]: the system is stable for all $\mathcal{T}$ for sufficiently low Reynolds numbers; for low $\mathcal{T}$ the critical Reynolds number for instability is constant and the oscillation is relatively low frequency; as $\mathcal{T}$ increases the critical Reynolds number for instability increases sharply before the neutral stability curve terminates abruptly (point of termination shown as an open circle in each case). As in a single flexible compartment channel, this point of termination corresponds to a loss of existence the lower stable branch of static wall profiles at a limit-point bifurcation (eg the static solution for $\mathcal{R} = 200$ in Fig. 2(b) inset exhibits a pair of saddle points). This interaction between an oscillatory Hopf bifurcation and a limit point bifurcation may lead to a global bifurcation and chaotic behaviour in the nearby parameter space [40]. In the four cases shown the neutral curves associated with modes (i) and (ii) remain relatively independent, although there is some evidence of mode interaction in Fig. 3(c) as the neutral curves deform toward one another.

Hence, the dimensionless model predicts that there are two distinct families of oscillation, either of which can form the primary global instability of the system depending on the parameters. The mode termed (i) has oscillatory behaviour evident in both compliant compartments, while the mode labelled (ii) involves oscillation only in the downstream compliant compartment.

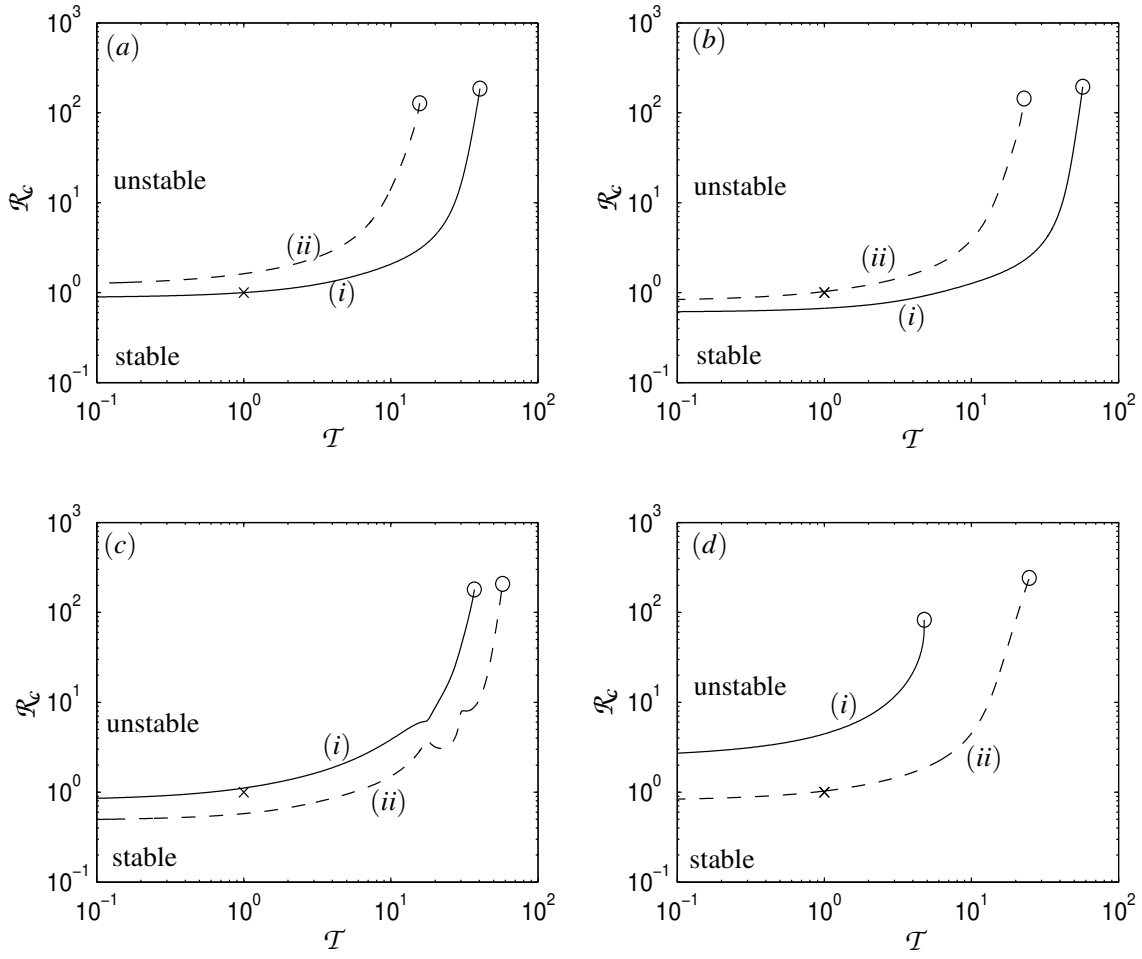


Figure 5: Neutrally stable oscillations of the system for fixed external pressures chosen as the four points labelled (a)-(d) in Fig. 3, showing in each case the critical Reynolds number for oscillation as a function of the (dimensionless) membrane tension: (a) $p_c = 100$, $p_e = 275$; (b) $p_c = 150$, $p_e = 400$; (c) $p_c = 250$, $p_e = 400$; (d) $p_c = 140$, $p_e = 200$. Here $\mathcal{L}_2 = \mathcal{L}_4 = 10$ and $\mathcal{L}_3 = 1$.

# 4 Application to the parameters of the retinal vein

We now apply the model constructed in Sec. 3 to the parameters pertinent to the central retinal vein to explore the conditions required for the onset of self-excited oscillations; we will then compare the predictions to measured data for the onset of RVp. Note that in this section we return to dimensional variables (unless otherwise stated). In particular we revisit the baseline case considered by [42], followed by an examination of the role of the vein wall tension (Sec. 4.4) and the inlet flow rate (Sec. 4.5). Although the model shows good qualitative agreement in the onset pressure conditions for RVp, there are several discrepancies (particularly in oscillation frequency) which are discussed in Sec. 4.6.

Following our previous paper [42], we consider a baseline case where $\mathcal{T} = 10$ ($T = 0.112$ N m$^{-1}$) with the other dimensional parameters as listed in Table 1. Note that this value of the membrane tension was been chosen to give qualitative agreement in the onset for low ICP, but no other fitting is involved. In Fig. 6 we trace neutral stability curves to elucidate the critical conditions required for the onset of self-excited oscillations as a function of the ICP. In particular, we plot the critical value of $P_e - P_0$ required for instability as a function of $P_c - P_0$ (Fig. 6a), along with corresponding frequency of neutrally stable oscillation (Fig. 6b). We explore the features of this baseline case below, focussing on the behaviour for low ICP (Sec. 4.1), large ICP (Sec. 4.2) and intermediate ICP (Sec. 4.3). We then progress to consider the role of varying the vein wall tension (Sec. 4.4) and the steady flow rate along the vein (Sec. 4.5).

It should be noted that the onset curve in Fig. 6(a) agrees well with the predictions of the onset of self-excited oscillations in our previous paper [42], with the onset points shown as open circles (Fig. 6a). The slight offset between the two predictions is because our previous fully nonlinear simulations used a time-dependent ICP where the predictions were reported in terms of the mean ICP rather than the range of values of $P_c - P_0$ for which the oscillations were actually evident. Comparing this onset curve to experimental measurements of the critical IOP required for the onset of RVp in canines (see Morgan *et al.* 2008 [33], with a summary of their data shown as a dotted line in Fig. 6(a)), we observe excellent qualitative (and even quantitative) agreement with the lower branch of our neutral stability curve along most of its length. In particular, the prediction faithfully reproduces the kink in the onset curve.

However, the current eigensolver approach provides access to a more complete description of the behaviour including explicit access to the oscillation frequency. The corresponding oscillation frequency of each of these neutral curves is shown in Fig. 6(b). The predicted (dimensional) oscillation frequency is very large (on the order of 500Hz), significantly larger than the frequency of RVp observed clinically (on the order of several Hz). Mathematically, this large oscillation frequency can be attributed to the relatively large value of the dimensional membrane tension (in a similar manner to previous studies [20, 40]). This suggests that although our model captures the critical conditions for the onset of oscillations, the frequency of instability is not well predicted. Possible improvements to the model to decrease the oscillation frequency toward physiologically realistic values are discussed in Sec. 4.6. However, motivated by the excellent agreement in the onset conditions for self-excited oscillations we continue to explore the parameter space to understand the onset of these oscillations in more detail.

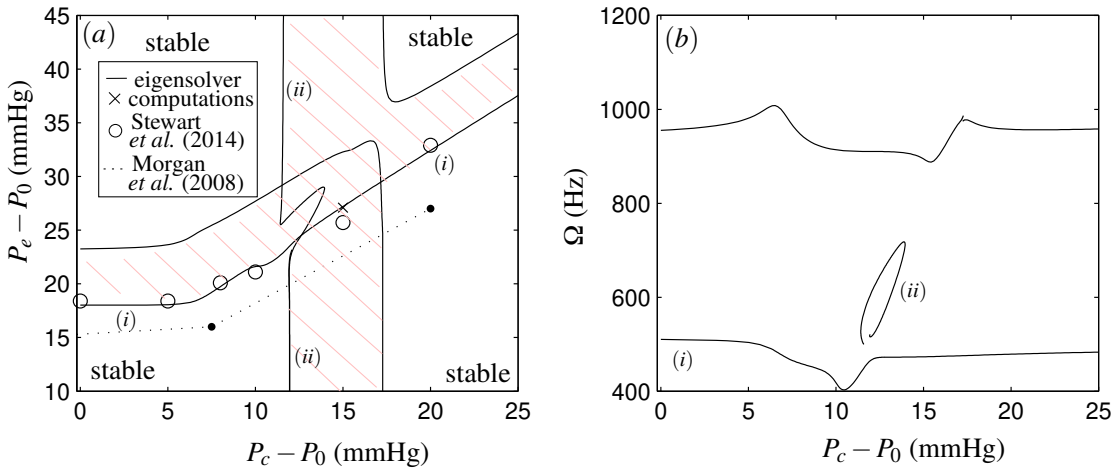


Figure 6: Neutrally stability curves for the onset of self-excited oscillations for $\mathcal{T} = 10$ plotted as a function of $P_c - P_0$: (a) the critical value of $P_e - P_0$ for the onset of instability; (b) the corresponding (dimensional) neutrally stable oscillation frequency. In (a) the points marked with open circles correspond to predictions of [42], the point marked with a cross is the predicted onset point from fully nonlinear simulations described in Fig. 7 and the dotted line is a summary of the measurements of RVp onset in canines from Morgan *et al.* (2008) [33]. All other parameter values are as listed in Table 1.

## 4.1 Low ICP

For sufficiently low IOP and ICP the system is stable to oscillations, as expected. Holding the ICP fixed $P_c = P_0$, increasing $P_e - P_0$ through a critical value ($\approx 18.0$mmHg) the system becomes unstable to self-excited oscillations (Fig. 6a) with critical frequency 510.1 Hz (Fig. 6b). In accordance with the dimensionless analysis above, we term this mode of instability mode (i), the primary mode of instability, as it persists for (almost) all values of the ICP (for sufficiently large IOP). The onset of this mode (i) is labelled in Fig. 6 and is consistent with our previous predictions [42] (open circles in Fig. 6a). However, the eigensolver approach gives access to further information. Continuing to increase the IOP, the model predicts that mode (i) eventually stabilises again across a second neutral curve (Fig. 6a). For example, for ICP fixed $P_c = P_0$ the system exhibits a critical pressure of $P_e - P_0 \approx 23.3$mmHg (Fig. 6a) with a larger critical frequency of 955.1Hz (Fig. 6b). The branch of solutions associated with the smaller (larger) critical ICP is termed the lower (upper) neutral branch of mode (i).

For these low ICP, the critical IOP for instability of mode (i) is approximately independent of the ICP. However, it is interesting to note that the two compartment system is predicted to be stable to oscillations above the upper branch, so the system is stable despite increasing the external pressurisation on compartment 1. Fully nonlinear simulations for $P_c = P_0$ corroborate this observation (not shown). A subsequent restabilisation of RVp at larger IOP has not been reported in the clinical literature. Reasons for this possible discrepancy are discussed in Sec. 5 below. However, we show below that eventually the system destabilises again for a much larger IOP.

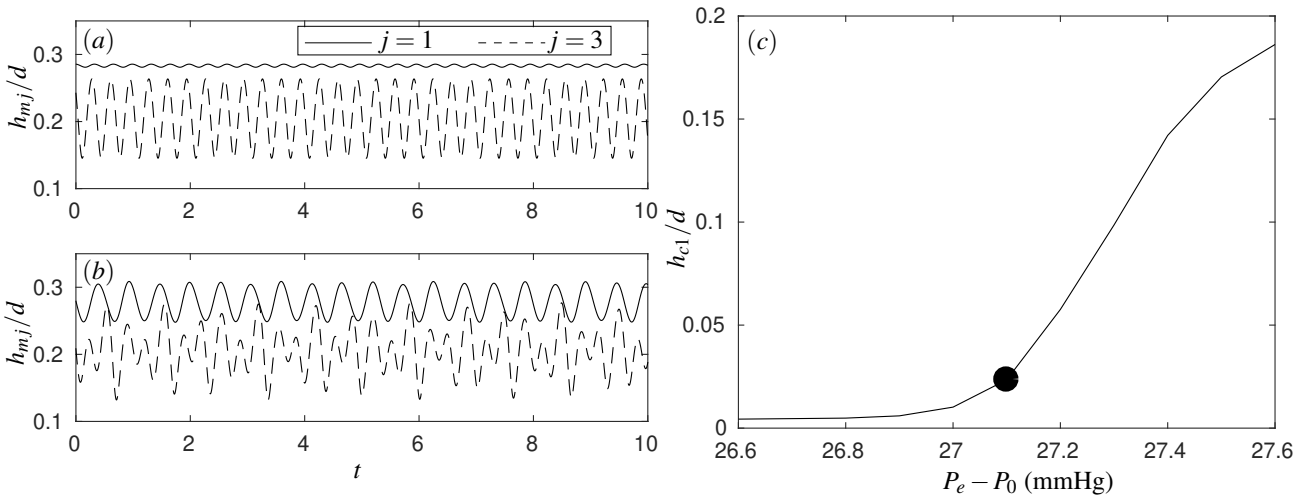


Figure 7: Fully nonlinear simulations of the onset of self-excited oscillation with $P_c - P_0 = 15$mmHg: (a) time-trace of the minimal channel width in compartment 1 (solid line) and compartment 3 (dashed line) for $P_e - P_0 = 27.0$mmHg; (b) time-trace of the minimal channel width in compartment 1 (solid line) and compartment 3 (dashed line) for $P_e - P_0 = 27.2$mmHg; (c) bifurcation diagram showing the amplitude of fully saturated oscillation as a function of $P_e - P_0$. The filled circle in (c) indicates the point where the oscillation in compartment (a) becomes significantly more prominent. All other parameters are chosen according to Table 1.

## 4.2 Large ICP

For large ICP the shape of the neutral stability curves is very different to those reported in Sec. 4.1. Tracking the neutral stability curves, the lower and upper branches still appear, but along both the critical IOP for (in)stability now scales linearly with the increasing ICP (Fig. 6a) while the corresponding frequency of oscillation approaches a constant value (Fig. 6b). This behaviour is again consistent with the canine experiments of [33].

## 4.3 Intermediate ICP

For intermediate values of ICP the behaviour of the system is significantly more complicated. As reported in the dimensionless analysis above, for fixed low IOP there is an additional oscillatory mode, which we term mode (ii), which becomes unstable across a range of ICP values. As shown in Fig. 6(a), the neutral stability curves for this mode (ii) persists for all IOP, so the instability has a fundamentally different character to mode (i), as expected. For example, for $P_e - P_0 = 10$mmHg we see onset of mode (ii) at $P_c - P_0 \approx 12.0$mmHg and subsequent restabilisation of this mode at $P_c - P_0 \approx 17.3$mmHg.

Along the upper branches of modes (i) and (ii) we observe an interchange in behaviour for $P_c - P_0 \approx 17.2$mmHg. This interchange is not explored here in detail, but we hypothesise that this arises due to a mode interaction between modes (i) and (ii) in the nearby parameter space.

To investigate the role of mode (ii) in the onset of visible self-excited oscillation in compartment 1, in Fig. 7 we consider fully nonlinear simulations across a range of $P_e$ close to the onset curve for fixed $P_c - P_0 = 15$mmHg, computing until the system has entered a fully saturated periodic limit

cycle. In particular, we illustrate time-traces of the minimal width of the channel in compartment 1 (solid line, the region visible to a clinician) and compartment 3 (dashed line) for $P_e - P_0 =$ 27.0mmHg (Fig. 7a) and for $P_e - P_0 =$27.2mmHg (Fig. 7b). In the former case, the oscillation in the minimal channel width in compartment 1 is present but almost invisible, whereas in the latter it is significantly more pronounced. As the IOP is further increased the system will eventually exhibit 'slamming' oscillations in one or both compartments, where over a period the channel transiently becomes highly constricted before recovering [41]. To quantify this behaviour formally we estimate the amplitude of the pulsation in compartment 1 as

$$h_{c1} = \max_t(h_{m1}) - \min_t(h_{m1}). \tag{19}$$

We trace the relative amplitude of the fully saturated oscillation in compartment 1 as a function of the IOP shown as the bifurcation diagram in Fig. 7(c). In this case, we see a dramatic shift in behaviour beyond a critical value of $P_e - P_0$, where the oscillation becomes much more evident. To quantify this point of onset we compute the point of maximal curvature of the trace of $h_{c1}$ as a function of $P_e - P_0$, estimated as $P_e - P_0 = 27.1$mmHg, plotted with a filled circle on Fig. 7(c). Furthermore, this point is also illustrated with a cross on Fig. 6(a), almost perfectly coincident with the onset curve for mode (i). Hence, although the dynamical system admits a second mode of instability which is unstable for all IOP across a range of ICP, the presence of this mode does not have a significant effect on the onset of (visible) self-excited oscillations in compartment 1.

Hence, the onset curve for the onset of self-excited oscillation can be viewed as the intersection of the behaviour for low ICP (where the critical IOP is independent of ICP, Sec. 4.1) and the behaviour for large ICP (where the critical IOP scales linearly with ICP, Sec. 4.2).

## 4.4 Varying the vein wall tension

The critical value of the IOP required for self-excited oscillation will be dependent on the value of the elastic wall tension, a model parameter which cannot be easily measured or estimated *in vivo*. In Fig. 8 we elucidate this dependency by tracing the critical IOP required for oscillatory instability (Fig. 8a) and the corresponding (dimensional) oscillation frequency (Fig. 8b) for various $P_c - P_0$ as a function of $\mathcal{T}$.

Firstly we consider low ICP, setting $P_c = P_0$. In this case, for low vein wall tensions (close to the baseline value) the critical IOP for mode (i) increases (linearly) as the tension increases. However, the instability does not persist as the tension is further increased: the neutral curve exhibits a turning point in the parameter space spanned by $(\mathcal{T}, P_e - P_0)$ and forms the upper branch of mode (i) described above. However, continuing to track this neutral curve it exhibits another turning point in the parameter space for much larger IOP and so the oscillatory instability eventually reappears for much larger IOP. Further numerical tests (not shown) indicate that this new unstable branch persists as the vein wall tension becomes very large. Along this neutral curve the critical frequency of oscillation scales with the square root of the dimensionless tension, consistent with the family of flux-driven oscillatory modes which persist for large tensions in a single compartment collapsible channel [40].

To explore how the critical conditions for instability at large ICP vary with the elastic wall tension, in Fig. 8(a) we plot the critical IOP for instability mode (i) as a function of the tension for $P_c = P_0 + 20$mmHg (dashed line). Similar to the case for mode (i) for low ICP, the critical IOP grows linearly with $\mathcal{T}$ for low tensions ($\mathcal{T} \lesssim 12$) but the critical curve again exhibits a turning point in the $(\mathcal{T}, P_e - P_0)$ parameter space, again corresponding to the upper branch of mode (i)

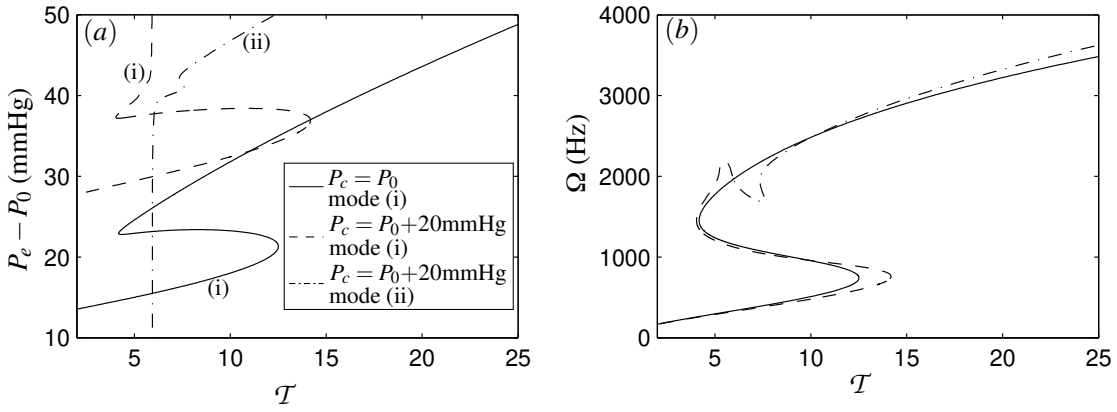


Figure 8: The onset of oscillation as a function of the vein wall tension $\mathcal{T}$: (a) the critical IOP for instability as a function of $\mathcal{T}$ holding $P_c - P_0 = 0$mmHg (solid line), $P_c - P_0 = 20$mmHg (dashed line for mode (i), dot-dashed line for mode (ii)); (b) the corresponding critical frequency of instability. All other parameters listed in Table 1.

for large ICP. As in the case of low ICP, the neutral curve eventually turns once again (through a rather complicated path) but now the critical IOP for instability approaches infinity for a constant value of the wall tension.

To further elucidate the critical conditions for onset of the secondary unstable mode (ii), in Fig. 8(a) we illustrate the critical IOP as a function of the wall tension for fixed ICP $P_c - P_0 = 20$mmHg. In this case we find that for low IOP the neutral curve asymptotes to a constant value of the tension. Conversely, for large $\mathcal{T}$ the critical IOP increases linearly with the tension, while the critical frequency increases as the square root of the tension (consistent with [40]).

This behaviour for large IOP appears rather contrary to our previous observations, where we might have expected that the critical IOP for mode (i) instability would increase linearly with the tension parameter (as in the case for $P_c = P_0$), while the critical IOP for mode (ii) instability would tend to infinity for a constant value of the tension (consistent with Fig. 6a). We speculate that this interchange of behaviour is due to a mode-interaction, where the neutral curves for modes (i) and (ii) have merged and separated again in different configuration.

## 4.5 Varying the flow rate along the vein

In Fig. 9 we investigate the dependency of the onset curve for self-excited oscillations on the magnitude of the steady flow rate entering the vein. In particular, in Fig. 9(a) we plot the onset curve for mode (i) oscillations (in the space spanned by the intracranial and intraocular pressures) for fluxes in the range 40-48$\mu$l min$^{-1}$ holding the dimensional elastic wall tension fixed at the baseline value ($T = 0.11$ Pa m$^{-1}$). It should be noted that changing $Q$ influences the mean flow through the vein $U_0$, so the dimensionless tension $\mathcal{T}$ will change for dimensional $T$ held fixed. We find that the behaviour for $Q = 40\mu$l min$^{-1}$ is qualitatively similar to $Q = 44\mu$l min$^{-1}$ (the baseline value considered above), although the curve is shifted to lower ICP and IOP, so in this space the system becomes more unstable as the flux is decreased. This prediction may seem counter-intuitive: as the Reynolds number of the flow decreases linearly with the flow rate, we might expect that this would make the system more stable rather than less for the same

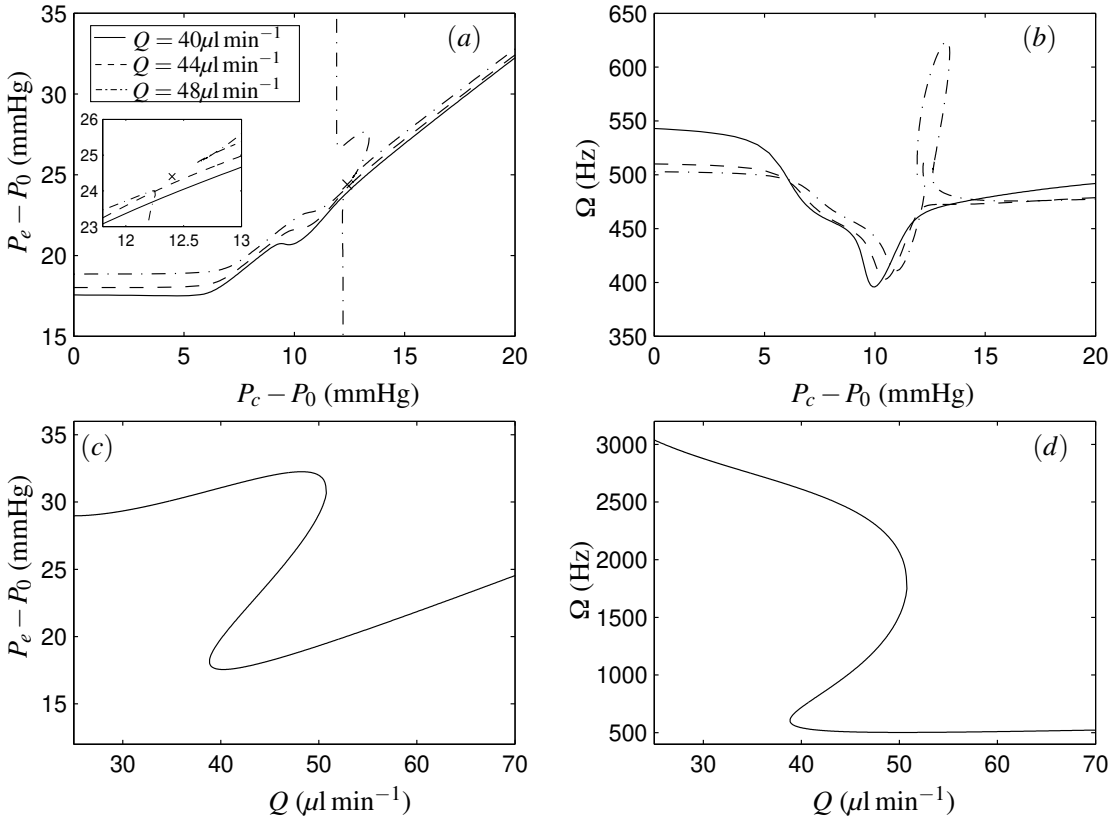


Figure 9: Predictions of the onset curve for self-excited oscillations while varying the steady flow rate into the vein: (a) the critical IOP for instability as a function of the ICP for $Q = 40$ $\mu$ l min$^{-1}$ (solid),$Q = 44$ $\mu$ l min$^{-1}$ (dashed) and $Q = 48$ $\mu$ l min$^{-1}$ (dot-dashed); (b) the corresponding frequency of oscillation for each of the neutral curves shown in (a); (c) the critical IOP for instability as a function of the steady flow rate through the vein of $P_c - P_0 = 0$mmHg; (d) the corresponding frequency of oscillation for the neutral curves shown in (c). The point marked with a cross in the inset of (a) is the onset point predicted from fully nonlinear simulations described in Fig. 10. All other parameters are chosen according to Table 1.

dimensional tension. We note that increasing $Q$ does, in fact, lead to a decrease in the critical dimensionless $p_e$, as expected (not shown). However, the (dimensional) inertial pressure scale along the channel ($\rho U_0^2$, see Eq. (1)) increases quadratically with increases in $Q$ and so the overall effect is a net increase in the critical (dimensional) IOP for onset of instability. The corresponding frequency of oscillation at onset is relatively unchanged (Fig. 9b). However, the onset curve for $Q = 48\mu\text{l}\,\text{min}^{-1}$ (Fig. 9) is subtly different. An interaction between modes (i) and (ii) leads to a different configuration of the onset curve. The portion along which IOP rises linearly with IOP now has a discontinuity across $P_c - P_0 \approx 12.2 - 12.6\text{mmHg}$, which may have implications for the onset of fully nonlinear oscillations; we explore this feature in more detail in Fig. 10 below.

To explore the onset of self-excited oscillations in cases of lower flow rates (such as in retinal vein occlusion [21, 47]), in Fig. 9(c,d) we plot the critical IOP for the onset of self-excited oscillations as a function of $Q$ holding the ICP fixed ($P_c = P_0$). It emerges that below a critical value of $Q$ (in this baseline case $Q \approx 38.9\mu\text{l min}^{-1}$), the family of mode (i) oscillations (discussed above, with critical IOP in the physiological range) ceases to exist. For these low fluxes the only possibility for instability is across a secondary neutral curve (still associated with mode (i)) evident for much larger values of the IOP.

To explore the complicated discontinuity in the mode (i) onset curve evident for $Q = 48\mu\text{l}\,\text{min}^{-1}$ (see Fig. 9a), in Fig. 10 we consider the neighbourhood of this discontinuity for $P_c - P_0 = 12.4\text{mmHg}$, showing fully nonlinear simulations of the behaviour in compartment 1 for $P_e - P_0 = 24.2\text{mmHg}$ (Fig. 10a) and $P_e - P_0 = 24.6\text{mmHg}$ (Fig. 10b). There is an evident increase in amplitude between these two cases (despite both being in the unstable regime), which we explore using a bifurcation diagram of $h_c$ (similar to Fig. 7c above). It emerges that there is a sharp transition in behaviour at $P_e - P_0 \approx 24.4\text{mmHg}$ (estimated in the same way as above and marked with a filled circle), where the oscillation in the vein wall in compartment 1 becomes significantly more visible. This point is plotted with a cross in the parameter space in Fig. 9(a). Interestingly, this onset point is almost directly in line with the two portions of the mode (i) onset branch where the IOP increases linearly with ICP. Hence, despite an extremely complicated underlying dynamical system the onset behaviour of RVp is essentially unchanged, where the IOP effectively increases linearly with ICP.

## 4.6 Assessing the modelling assumptions for application to RVp onset

In the earlier parts of this section we demonstrated good qualitative agreement between the predictions of our model and the onset of RVp measured in canines, using the wall membrane tension as a fitting parameter. The model predictions faithfully reproduce the kink in the onset curve in the parameter space spanned by the two external pressures and highlight the two distinct regions for large and small ICP. However, the model predictions of the oscillation frequency are several orders of magnitude larger than clinical observations. We now revisit the modelling assumptions to assess the modifications that may be required to produce a more realistic prediction of the oscillation frequency.

Firstly, our model treats the vein as a flexible-walled channel rather than a collapsible tube. Such an approximation has been shown to encompass many of the same mechanisms of self-excited oscillation (eg. the 3D tube model of Whittaker and coworkers [45] demonstrated essentially the same mechanism of instability as the channel system [20]). However, the influence of azimuthal flows and non-axissymmetric buckling of the tube wall could have an influence on the predictions.

Secondly, we modelled the vein wall as a tensioned membrane, neglecting the influence of wall

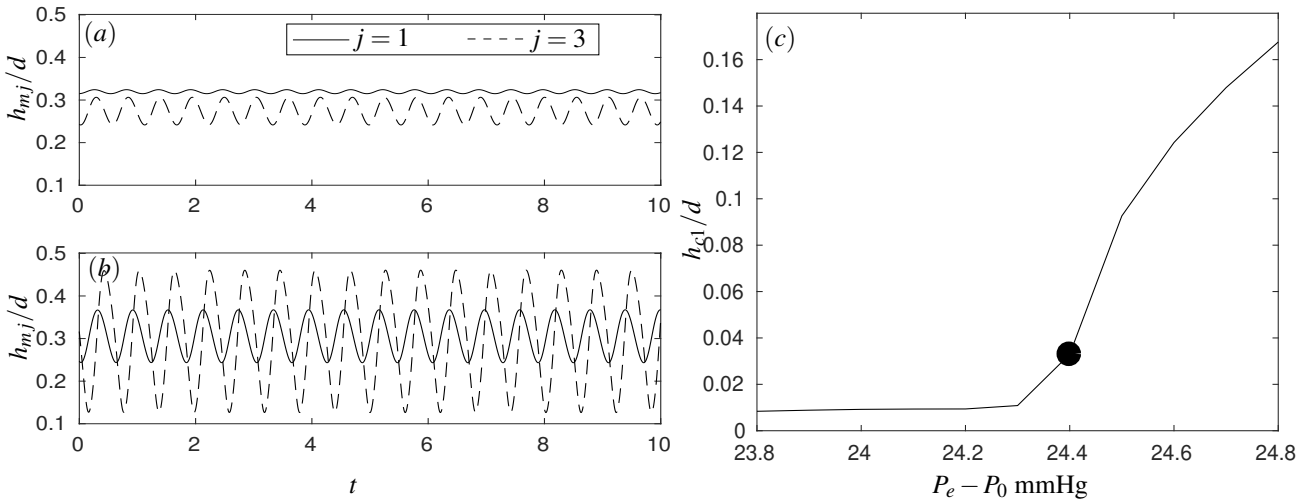


Figure 10: Fully nonlinear simulations of self-excited oscillations close to the discontinuity in the onset curve for $Q = 48\mu\mathrm{l\,min}^{-1}$ and $P_c - P_0 = 12.4$mmHg: (a) time-trace of the minimal channel width in compartment 1 (solid line) and compartment 3 (dashed line) for $P_e - P_0 = 24.2$mmHg; (b) time-trace of the minimal channel width in compartment 1 (solid line) and compartment 3 (dashed line) for $P_e - P_0 = 24.6$mmHg; (c) bifurcation diagram of the amplitude of fully-developed oscillation in compartment 1 as a function of $P_e - P_0$. The filled circle in (c) illustrates the change in behaviour, where the self-excited oscillations in compartment 1 become significantly more prominent. All other parameters chosen according to Table 1.

inertia, bending stiffness and viscoelastic effects. Such an approach is motivated by the collapsible channels literature where the aim is to keep the wall model simple to better understand the mechanism(s) of oscillation (eg. [20,43,43]) but such an approach may miss features of the physiological problem. In this context we essentially assume that the axial membrane tension dominates these other effects. The literature estimates the Young's modulus of the central retinal vein as $E = 0.6$MPa, which translates into a stiffness parameter of approx 40Pa [39]. Our chosen value of the membrane tension parameter ($\approx$0.11 N m$^{-1}$) correlates to pressure of $\approx$ 362Pa (using the radius of the vein as a typical lengthscale), so our assumption is at least self-consistent. However, we recognise that changes to the wall tension parameter may adjust this balance, especially as the wall model becomes more complicated.

This assumption of a tension dominated wall model also has consequences for the oscillation frequency. In single compartment models the oscillation frequency typically becomes large when the dimensionless tension parameter $\mathcal{T}$ exceeds unity (observed for either flow-driven or pressure-driven cases [20,40,43]), scaling as $\mathcal{T}^{1/2}$ in the limit as $\mathcal{T} \to \infty$. This scaling is evident in our case in Fig. 8. Hence, given our fitted wall tension parameter corresponds to a dimensionless value $\mathcal{T} = 10$ (used in Fig. 6), this helps to explain why the predicted oscillation frequency is so large. To increase the agreement with the clinical observations it is therefore necessary to increase the complexity of the wall model. For example, preliminary simulations including the effects of wall inertia have been shown to reduce the frequency of oscillation considerably, but a much wider parameter sweep is necessary to reduce the frequency to the physiological regime.

Thirdly, the present model neglects oscillations in the external pressures (IOP and ICP) driven by the cardiac cycle; these external forcing oscillations were included in our previous model [42] making no qualitative (and little quantitative) difference to the results. However, it should be noted that resonant effects between the forced and self-excited oscillations may be promoted if the wall model is substantially modified to decrease the frequency of self-excited oscillation.

In addition, we modelled the inlet to the retinal vein with a fixed flow rate, neglecting any coupling to the cardiac cycle. This assumption presumes that the generated pressure oscillations are typically very small amplitude compared to the overall pressure drop between the heart and the upstream end of the retinal vein. Taking an average pressure in the heart as 100 mmHg, typical estimates of blood pressure entering the central retinal vein are $\approx$ 15mmHg, giving a pressure difference of $\approx$ 85mmHg. There are no direct measurements of the oscillating RVp pressure (to the best of our knowledge), it seems but in our nonlinear simulations in Fig. 7 the model predicts an oscillatory pressure amplitude of $\approx$ 0.08mmHg (as the vein leaves the eye), so our model is at least self-consistent.

Finally, we have ignored the influence of tapering of the vein so that the steady flow is everywhere constant along its length. This, coupled to our assumption that the inlet flow into the vein is always constant despite changes in IOP and/or ICP, means that the model predicts the oscillations subsequently stabilise as the IOP is increased (Fig. 6), before eventually becoming unstable again for much larger IOP (Fig. 8). Such a re-stabilisation of RVp has not been observed clinically and we expect that a model where the inlet flow rate were coupled to the ICP and/or IOP would be required to eradicate this behaviour. However, such a model would require consideration of the flow through the entire retinal circulation (including the arterial side and the influence of auto-regulation [14]) which is beyond the scope of the present study and deferred to future work.

# 5 Discussion

In this paper we have considered a theoretical model for the flow along a long flexible-walled channel which comprises two flexible compartments in series separated by a long rigid compartment. The flow is driven by a fixed upstream flux against a fixed downstream pressure. This channel is externally exposed to different external pressures on each flexible compartment, and the resulting onset of self-excited oscillations exhibits an interesting coupling between these two pressures. In particular, we formulated a system of PDEs to describe the fluid mechanics coupled to the displacement of the channel wall, assuming the elastic response is dominated by a large membrane tension. The system was considerably simplified using a long-wavelength approximation coupled to a prescribed flow profile (everywhere parabolic). Such assumptions are justified given the large aspect ratio of the retinal vein across the region of interest and the relatively low Reynolds numbers of the flow.

To isolate the onset of self-excited oscillations we formulated a global (linear) stability eigensolver, similar to the approach of [40]. We found that the primary global instability of this system was to one of two oscillatory modes depending on the parameters, termed modes (i) and (ii): in mode (i) the eigenmode involved oscillations of similar amplitude in both compliant compartments, while in mode (ii) the eigenmode was strongly dominated by the response in the downstream compliant compartment (Fig. 4). Hence, for these boundary conditions it is possible to see oscillations in the downstream compartment alone (to a first approximation), while any significant oscillation in the upstream flexible compartment must be coupled to oscillations of comparable amplitude in the downstream compliant compartment. This correlates to the static behaviour of the system, where we showed that for these boundary conditions the static deformation of the downstream compliant compartment is entirely independent of the upstream compliant compartment, while the static deformation of the upstream flexible compartment is necessarily driven by the shape of the downstream compliant compartment.

Applying our model to the parameters and geometry of the central retinal vein (Table 1) and assuming that the external pressure on the upstream (downstream) compliant comparmtent is the IOP (ICP), the onset curve for mode (i) oscillations shows strong qualtitative agreement with the onset of RVp in the canine experiments of Morgan *et al.* (2008) [33] (Fig. 6a). In producing a comparison we have chosen the value of the wall tension parameter to give good agreement in onset at low ICP. Using this one fitting parameter, the model faithfully reproduces the kink in the onset curve which is observed in RVp onset measurements in canines, dividing the onset curve into two regimes - one where the critical IOP is constant (for low ICP) and one where it increases linearly with ICP (for large ICP). However, the corresponding oscillation frequency is much larger than clinical observations, which we attribute to the simplicity of our wall model (see extended discussion in Sec. 4.6).

Furthermore, we showed that in some cases the underlying dynamical system exhibits significant complexity including superposition and interaction of modes (i) and (ii) which can alter the shape of the neutral stability curves (Fig. 10). However, despite these complications, fully nonlinear simulations indicated that the onset curve for oscillations which would be visible in the upstream flexible compartment remains remarkably simple and in line with the experimental predictions discussed above (Fig. 7).

Furthermore, we used our eigensolver approach to fully explore the parameter space, showing that the onset of oscillations can be delayed to significantly larger IOP (with a significant increase in the corresponding frequency of oscillation) if the flow rate along the vein is reduced. Such a

reduction in flow rate may occur in cases of retinal vein occlusion [21, 47], where delayed onset of RVp may provide a useful clinical indicator.

## Acknowledgements

Helpful discussions with Prof. O. E. Jensen (University of Manchester, UK) are very gratefully acknowledged. PSS gratefully acknowledges funding from EPSRC grant nos. EP/N014642/1 and EP/P024270/1.

## Data

Numerical codes used for generating the data in this paper can be accessed at
`http://dx.doi.org/10.5525/gla.researchdata.845`

# References

[1] J. P. Armitstead, C. D. Bertram, and O. E. Jensen. A study of the bifurcation behaviour of a model of flow through a collapsible tube. *Bull. Math. Biol.*, 58(4):611–641, 1996.

[2] L. R. Band, C. L. Hall, G. Richardson, O. E. Jensen, J. H. Siggers and A. J. E. Foss. Intracellular flow in optic nerve axons: a mechanism for cell death in glaucoma. *Invest. Ophthalmol. Vis. Sci.*, 50(8):3750–3758, 2009.

[3] C. D. Bertram and T. J. Pedley. A mathematical model of unsteady collapsible tube behaviour. *J. Biomech.*, 15(1):39–50, 1982.

[4] C. D. Bertram, C. J. Raymond, and T. J. Pedley. Mapping of instabilities for flow through collapsed tubes of differing length. *J. Fluids Struct.*, 4(2):125–153, 1990.

[5] C. D. Bertram and J. Tscherry. The onset of flow-rate limitation and flow-induced oscillations in collapsible tubes. *J. Fluids Struct.*, 22:1029–1045, 2006.

[6] C. Cancelli and T. J. Pedley. A separated-flow model for collapsible-tube oscillations. *J. Fluid Mech.*, 157:375–404, 1985.

[7] C. Davies and P. W. Carpenter. Instabilities in a plane channel flow between compliant walls. *J. Fluid Mech.*, 352: 205–243, 1997.

[8] C. Davies and P. W. Carpenter. Numerical simulation of the evolution of Tollmien–Schlichting waves over finite compliant panels. *J. Fluid Mech.*, 335: 361–392, 1997.

[9] E. A. Coccius. *Ueber die Anwendung des Augen-Spiegels: nebst Angabe eines neuen Instrumentes*. Müller, 1853.

[10] G. Garhofer, R. Werkmeister, N. Dragostinoff, and L. Schmetterer. Retinal blood flow in healthy young subjects. *Invest. Ophthalmol. Vis. Sci.*, 53(2):698–703, 2012.

[11] S. M. Golzan, S. L. Graham, J. Leaney, and A. Avolio. Dynamic association between intraocular pressure and spontaneous pulsations of retinal veins. *Curr. Eye Res.*, 36(1):53–59, 2011.

[12] S. M. Golzan, M. O. Kim, A. S. Seddighi, A. Avolio, and S. L. Graham. Non-invasive estimation of cerebrospinal fluid pressure waveforms by means of retinal venous pulsatility and central aortic blood pressure. *Ann. Biomed. Engng.*, 40(9):1940–1948, 2012.

[13] J. B. Grotberg and O. E. Jensen. Biofluid Mechanics in Flexible Tubes. *Ann. Rev. Fluid Mech.*, 36:121–147, 2004.

[14] G. Guidoboni, A. Harris, S. Cassani, J. Arciero, B. Siesky, A. Amireskandari, L. Tobe, P. Egan, I. Januleviciene, and J. Park. Intraocular pressure, blood pressure, and retinal blood flow autoregulation: a mathematical model to clarify their relationship and clinical relevance. *Invest. Ophthalmol. Vis. Sci.*, 55(7),4105–4118, 2014.

[15] A. Hartmann. Non-invasive measurement of intracranial pressure. *Lancet*, 351(9101):524, 1998.

[16] S. S. Hayreh. The central artery of the retina its role in the blood supply of the optic nerve. *The British journal of ophthalmology*, 47(11):651, 1963.

[17] M. Heil and J. Boyle. Self-excited oscillations in three-dimensional collapsible tubes: simulating their onset and large-amplitude oscillations. *J. Fluid Mech.*, 652:405–426, 2010.

[18] M. Heil and A. L. Hazel. Fluid-structure interaction in internal physiological flows. *Ann. Rev. Fluid Mech.*, 43:141–162, 2011.

[19] O. E. Jensen. Instabilities of flow in a collapsed tube. *J. Fluid Mech.*, 220:623–659, 1990.

[20] O. E. Jensen and M. Heil. High-frequency self-excited oscillations in a collapsible-channel flow. *J. Fluid Mech.*, 481:235–268, 2003.

[21] J. Jonas, M. Paques, J. Monés, and A. Glacet-Bernard. Retinal vein occlusions. In *Macular Edema*, volume 47, pages 111–135. Karger Publishers, 2010.

[22] J. B. Jonas. Retinal venous pulsation and glaucoma. *Ophthalmol.*, 112(5):948–949, 2005.

[23] M. O. Kramer. Boundary layer stabilization by distributed damping. *J. Am. Soc. Naval Eng.*, 72(1): 25–34, 1960.

[24] B. E. Levin. The clinical significance of spontaneous pulsations of the retinal vein. *Arch. Neurol.*, 35(1):37–40, 1978.

[25] D. N. Levine. Spontaneous pulsation of the retinal veins. *Microvas. Res.*, 56(3):154–165, 1998.

[26] X. Y. Luo, Z. X. Cai, W. G. Li, and T. J. Pedley. The cascade structure of linear instability in collapsible channel flows. *J. Fluid Mech.*, 600:45–76, 2008.

[27] X. Y. Luo, and T. J. Pedley. A numerical simulation of unsteady flow in a two-dimensional collapsible channel. *J. Fluid Mech.*, 314:191–225, 1996.

[28] X. Y. Luo, T. J. Pedley. The effects of wall inertia on flow in a two-dimensional collapsible channel. *J. Fluid Mech.*, 363:253–280, 1998.

[29] M. E. McClurken, I. Kececioglu, R. D. Kamm, and A. H. Shapiro. Steady, supercritical flow in collapsible tubes. Part 2. Theoretical studies. *J. Fluid Mech.*, 109:391–415, 1981.

[30] S. Moghimi, H. Hosseini, J. Riddle, G. Y. Lee, E. Bitrian, J. Giaconi, J. Caprioli, and K. Nouri-Mahdavi. Measurement of optic disc size and rim area with spectral-domain OCT and scanning laser ophthalmoscopy. *Invest. Ophthalmol. Vis. Sci.*, 53:45194530, 2012.

[31] W. H. Morgan, M. L. Hazelton, S. L. Azar, P. H. House, D.-Y. Yu, S. J. Cringle, and C. Balaratnasingam. Retinal venous pulsation in glaucoma and glaucoma suspects. *Ophthalmol.*, 111(8):1489–1494, 2004.

[32] W. H. Morgan, M. L. Hazelton, and D.-Y. Yu. Retinal venous pulsation: Expanding our understanding and use of this enigmatic phenomenon. *Prog. Ret. Eye Res.*, 55:82–107, 2016.

[33] W. H. Morgan, D.-Y. Yu, and C. Balaratnasingam. The role of cerebrospinal fluid pressure in glaucoma pathophysiology: the dark side of the optic disc. *J. Glaucoma*, 17(5):408–413, 2008.

[34] T. J. Pedley. *The fluid mechanics of large blood vessels.* Cambridge University Press, 1980.

[35] D. Pihler-Puzović, and T. J. Pedley. Flutter in a quasi-one-dimensional model of a collapsible channel. *Proc. R. Soc. A*, 470:2166, 2014.

[36] P. K. Sen, P. W. Carpenter, S. Hegde and C. Davies. A wave driver theory for vortical waves propagating across junctions with application to those between rigid and compliant walls. *J. Fluid Mech.*, 625:1–46, 2009.

[37] S. Singh and R. Dass. The central artery of the retina I. Origin and course. *Br. J. Ophthalmol.*, 44(4):193, 1960.

[38] S. Singh and R. Dass. The central artery of the retina II. A study of its distribution and anastomoses. *Br. J. Ophthalmol.*, 44(5):280, 1960.

[39] T. A. Spelman & P. S. Stewart. Shock wave propagation along the central retinal blood vessels *submitted*

[40] P. S. Stewart. Instabilities in flexible channel flow with large external pressure. *J. Fluid Mech.*, 825:922–960, 2017.

[41] P. S. Stewart, M. Heil, S. L. Waters, and O. E. Jensen. Sloshing and slamming oscillations in collapsible channel flow. *J. Fluid Mech.*, 662:288–319, 2010.

[42] P. S. Stewart, O. E. Jensen, and A. J. E. Foss. A theoretical model to allow prediction of the CSF pressure from observations of the retinal venous pulse. *Invest. Ophthalmol. Vis. Sci.*, 55(10):6319–6323, 2014.

[43] P. S. Stewart, S. L. Waters, and O. E. Jensen. Local and global instabilities of flow in a flexible-walled channel. *Eur. J. Mech. B*, 28(4):541–557, 2009.

[44] T. J. Walsh, J. W. Garden, and B. Gallagher. Obliteration of retinal venous pulsations: During elevation of cerebrospinal-fluid pressure. *Am. J. Ophthalmol.*, 67(6):954–956, 1969.

[45] R. J. Whittaker, M. Heil, O. E. Jensen, and S. L. Waters. A rational derivation of a tube law from shell theory. *Quart. J. Mech. Appl. Math.*, 63(4):465–496, 2010.

[46] T. H. Williamson, G. D. Lowe, and G. M. Baxter. Influence of age, systemic blood pressure, smoking, and blood viscosity on orbital blood velocities. *Br. J. Ophthalmol.*, 79(1):17–22, 1995.

[47] T. Y. Wong and I. U. Scott. Retinal-vein occlusion. *New Eng. J. Med.*, 363(22):2135–2144, 2010.

[48] X. Xie, X. Zhang, J. Fu et al. Noninvasive intracranial pressure estimation by orbital subarachnoid space measurement: the Beijing intracranial and intraocular pressure (iCOP) study. *Crit. Care*, 17(4):R162, 2013.

[49] F. Xu, J. Billingham, and O. E. Jensen. Divergence-driven oscillations in a flexible-channel flow with fixed upstream flux. *J. Fluid Mech.*, 723:706–733, 2013.

[50] F. Xu, J. Billingham, and O. E. Jensen. Resonance-driven oscillations in a flexible-channel flow with fixed upstream flux and a long downstream rigid segment. *J. Fluid Mech.*, 746:368–404, 2014.

[51] F. Xu and O. E. Jensen. A low-order model for slamming in a flexible-channel flow. *Quart. J. Mech. Appl. Math.*, 68(3):299–319, 2015.